Structural and functional analysis of AsbF: Origin of the stealth 3,4-dihydroxybenzoic acid subunit for petrobactin biosynthesis

Brian F. Pfleger[a], Youngchang Kim[b], Tyler D. Nusca[a,c], Natalia Maltseva[b], Jung Yeop Lee[a], Christopher M. Rath[a], Jamie B. Scaglione[a], Brian K. Janes[c], Erica C. Anderson[c], Nicholas H. Bergman[d], Philip C. Hanna[c], Andrzej Joachimiak[b,e], and David H. Sherman[a,c,1]

[a]Life Sciences Institute and Departments of Medicinal Chemistry and Chemistry, University of Michigan, 210 Washtenaw Avenue, Ann Arbor, MI 48109; [b]Midwest Center for Structural Genomics and Structural Biology Center, Biosciences Division, Argonne National Laboratory, 9700 South Cass Avenue, Building 202, Argonne, IL 60439; [e]Department of Biochemistry and Molecular Biology, University of Chicago, 920 East Fifty-Eighth Street, Chicago, IL 60637; [c]Department of Microbiology and Immunology, University of Michigan Medical School, Ann Arbor, MI 48109; and [d]School of Biology, Georgia Institute of Technology and Electro-Optical Systems Laboratory, Georgia Tech Research Institute, 310 Ferst Drive, Atlanta, GA 30332-0230

Petrobactin, a virulence-associated siderophore produced by *Bacillus anthracis*, chelates ferric iron through the rare 3,4-isomer of dihydroxybenzoic acid (3,4-DHBA). Most catechol siderophores, including bacillibactin and enterobactin, use 2,3-DHBA as a biosynthetic subunit. Significantly, siderocalin, a factor involved in human innate immunity, sequesters ferric siderophores bearing the more typical 2,3-DHBA moiety, thereby impeding uptake of iron by the pathogenic bacterial cell. In contrast, the unusual 3,4-DHBA component of petrobactin renders the siderocalin system incapable of obstructing bacterial iron uptake. Although recent genetic and biochemical studies have revealed selected early steps in petrobactin biosynthesis, the origin of 3,4-DHBA as well as the function of the protein encoded by the final gene in the *B. anthracis* siderophore biosynthetic (*asb*) operon, *asbF* (BA1986), has remained unclear. In this study we demonstrate that 3,4-DHBA is produced through conversion of the common bacterial metabolite 3-dehydroshikimate (3-DHS) by AsbF—a 3-DHS dehydratase. Elucidation of the cocrystal structure of AsbF with 3,4-DHBA, in conjunction with a series of biochemical studies, supports a mechanism in which an enolate intermediate is formed through the action of this 3-DHS dehydratase metalloenzyme. Structural and functional parallels are evident between AsbF and other enzymes within the xylose isomerase TIM-barrel family. Overall, these data indicate that microbial species shown to possess homologs of AsbF may, like *B. anthracis*, also rely on production of the unique 3,4-DHBA metabolite to achieve full viability in the environment or virulence within the host.

AsbF structure | dehydratase | siderophore | virulence factor

Siderophore production in pathogenic bacteria has gained considerable attention because of its crucial function in essential iron uptake by many microbes and the relevance of siderophore-associated proteins as molecular markers of various infectious agents (1). In *Bacillus anthracis*, the causative agent of anthrax, 2 siderophores, petrobactin and bacillibactin (Fig. 1*A*), play a significant role during iron acquisition (2–4), but only petrobactin is absolutely essential for full virulence within a mammalian host (5). This siderophore was initially discovered from the Gram-negative marine bacterium *Marinobacter hydrocarbonoclasticus*, whose genome bears a biosynthetic gene cluster homologous to the *B. anthracis asb* operon (2). Recent genetic and chemical analysis suggests that petrobactin biosynthesis may also be a prerequisite for virulence in related *Bacillus* species (6). These studies highlight the importance of elucidating the mechanisms of siderophore production in pathogenic microbes as a target for abrogating infection by organisms like *B. anthracis*, a rapidly virulent microbe with proven potential as a bioterrorism agent. Based on these factors, we have initiated studies to investigate key biosynthetic enzymes for petrobactin assembly in efforts to establish new antimicrobial targets to protect against anthrax. Eliminating petrobactin in pathogenic microbes is particularly important among catecholate siderophores, because the 3,4-dihydroxybenzoic acid (3,4-DHBA) moiety enables the molecule to escape sequestration by the mammalian immune protein siderocalin (7, 8). However, the genes responsible for mediating production of this metabolic precursor have remained undefined, as has the biochemical mechanism of its assembly.

Biosynthesis of petrobactin in *B. anthracis* requires citrate, spermidine, and 3,4-DHBA as biosynthetic units (3, 9). Whereas citrate and spermidine are readily available primary metabolites in bacteria, the presence of a 3,4-DHBA in the precursor pool is unusual. Because 3,4-DHBA is critical for petrobactin to function as a virulence factor, we hypothesized that the *asb* operon would likely code for its synthesis. Indeed, it was indicated by earlier reports (10), by precursor incorporation studies (11), and through our own analysis that supernatants of a *B. anthracis* Sterne culture contain 3,4-DHBA. Specifically, we demonstrated that supernatants of an *asbABCDEF* mutant fail to accumulate this key petrobactin subunit, indicating that 1 or more *asb*-encoded polypeptides are involved in its synthesis. Further examination of supernatants isolated from cultures of individual *asb* deletion mutants (3) revealed that each strain is capable of producing 3,4-DHBA except Δ*asbF*. To substantiate its functional role, we sought to determine the biochemical function of recombinant AsbF exogenously expressed and purified from *Escherichia coli*. X-ray crystallographic analysis of AsbF provides structural details of this unique polypeptide and has enabled new insights into AsbF enzymatic activity and a proposed mechanism in formation of the 3,4-DHBA moiety essential to petrobactin biosynthesis. Moreover, this study identifies AsbF as a potential new target in efforts to identify inhibitors for development of effective therapeutics against *B. anthracis* and
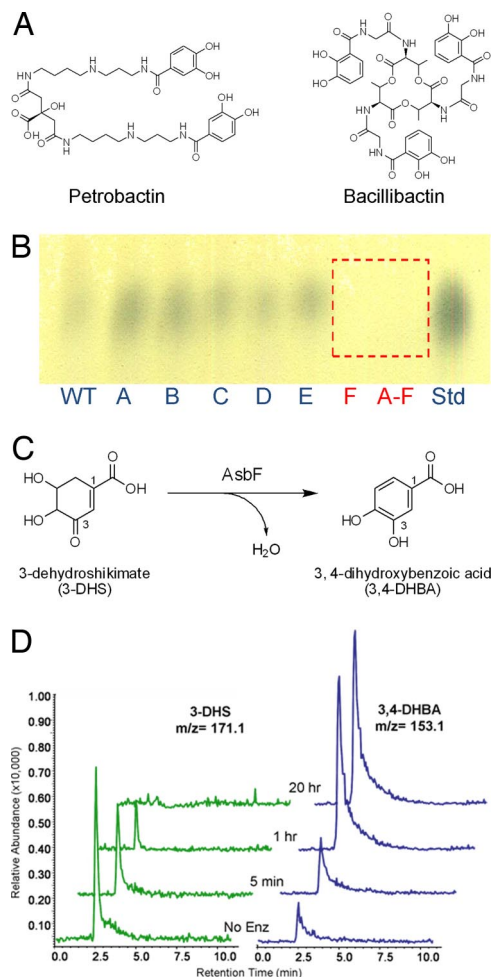
Fig. 1. AsbF catalyzes dehydration of 3-DHS to 3,4-DHBA in *B. anthracis*. (*A*) Structures of petrobactin and bacillibactin, 2 siderophores of *B. anthracis*. (*B*) TLC analysis of culture supernatants from Δ*asb* mutant strains stained with FeCl$_3$. All strains generated a spot that comigrated with an authentic 3,4-DHBA standard except Δ*asbABCDEF* and Δ*asbF*. (*C*) Chemical transformation showing the dehydration of 3-DHS, a common bacterial metabolite, to generate the unique siderophore precursor 3,4-DHBA. (*D*) LC-MS traces of the AsbF reaction quenched at sequential time points to illustrate conversion of 3-DHS to 3,4-DHBA. No Enz, no enzyme control incubated for 20 h.

other pathogens where petrobactin operates as a stealth virulence factor.

Results and Discussion

The Requirement for AsbF Is Revealed Through Analysis of *B. anthracis* Mutant Strains. The role of AsbF was initially assessed by determining the level of 3,4-DHBA production from various *B. anthracis* strains, including Δ*asbA*, Δ*asbB*, Δ*asbC*, Δ*asbD*, Δ*asbE*, Δ*asbF*, and Δ*asbABCDEF* (3), as well as a wild-type Sterne 34F2, that were grown in iron-depleted medium (IDM) (3). The presence of 3,4-DHBA was assayed by cellulose plate TLC on organic solvent extracts obtained from filtrates of the IDM cultures of each strain. TLC analysis revealed a single spot corresponding to the iron-chelating compound 3,4-DHBA evident in the extracts of *B. anthracis* Sterne 34F$_2$ and the mutants Δ*asbA*, Δ*asbB*, Δ*asbC*, Δ*asbD*, and Δ*asbE* at R_f = 0.91–0.93 (Fig. 1*B*). In contrast, spots corresponding to the subunit were absent in the Δ*asbF* and Δ*asbABCDEF* strains. The ferri-DHBA complex is a strong chromophore, forming blue-colored complexes when sprayed with 1% FeCl$_3$ after TLC development. Extract

samples were further analyzed with HPLC by using a C18 reverse-phase semipreparative column. The retention time and UV spectrum of the corresponding 3,4-DHBA peaks in each sample were coincident with an authentic standard (data not shown). Peak areas were determined, quantified, and compared based on a standard curve constructed by injecting a series of 6 concentrations (ranging from 0 to 500 μg/mL) of authentic 3,4-DHBA [supporting information (SI) Table S1]. Analysis of these *B. anthracis* mutants provided compelling evidence for the function of the BA1986 gene product (AsbF) as the 3,4-DHBA synthase necessary for petrobactin production. Moreover, in a mouse model of inhalation anthrax (12), the Δ*asbF* mutant strain was found to be completely avirulent at day 10, whereas the parental Sterne strain (34F2) resulted in 50% fatality over the same period (Fig. S1).

Bioinformatic analysis revealed that the *asb* cluster is conserved in a variety of bacterial genomes, including both Gram-positive and Gram-negative organisms (Fig. S2*A*). Interestingly, these microbes do not share a common niche; they are found in diverse environments with marine species dominating. The significance of this trend is unclear because it is difficult to assess how widespread petrobactin synthesis is within marine bacterial genomes. However, the relative phylogenetic diversity of bacteria bearing an *asb*-type operon (Fig. S2*B*), together with evidence that these gene clusters appear to have been acquired long ago (they have diverged considerably in sequence, and each has assumed the global sequence characteristics of its host genomes), suggests that petrobactin may confer a competitive advantage in iron acquisition within the ocean environment as well. We expect that as the number of sequenced bacterial genomes increases, the evolutionary history of the *asb* cluster will become clearer, and clues to the significance of petrobactin in various habitats will emerge.

AsbF Is Responsible for Conversion of 3-Dehydroshikimate (3-DHS) to 3,4-DHBA. To guide our initial studies of AsbF catalytic activity, bioinformatic analyses were conducted to identify potential functional homologs and to suggest reaction substrates. However, these efforts revealed only sequence similarity to conserved proteins of unknown function or irrelevant catalytic properties (data not shown). Alternatively, a search of the biochemical pathway databases revealed several anabolic processes leading to assembly of 3,4-DHBA, in addition to the many well studied catabolic pathways. In some bacteria (exemplified by *Pseudomonas putida* PobA), 3,4-DHBA is generated by hydroxylation of 4-hydroxybenzoic acid (4-HBA) to use the substrate as a carbon source (13). However, reaction of purified AsbF with 4-HBA and NAD(P)H failed to yield 3,4-DHBA (data not shown).

We considered an alternative metabolic process found in *Neurospora crassa* (*qa-4*), *Aspergillus nidulans* (*QutC*), and *Klebsiella pneumoniae* (*aroZ*) where 3,4-DHBA is generated by dehydration of 3-dehydroshikimate (3-DHS), a shikimate pathway intermediate, to use aromatic compounds as a carbon source (Fig. 1*C*) (14–16). A reaction mixture including AsbF with 3-DHS (purified from cultures of recombinant *E. coli*) (17) resulted in a product bearing a new absorbance maximum at 290 nm that corresponded to a DHBA chromophore (Fig. S3*A*). Upon analysis by LC-MS in negative SIM mode, the same reaction mixture resulted in disappearance of 3-DHS (m/z = 171) and generation of a product consistent with the structure of 3,4-DHBA (m/z = 153) (Fig. 1*D*). Both starting material and product eluted from a C18 reverse-phase column with retention times identical to authentic standards (data not shown).

Enzymatic Characterization. With a clear catalytic role for AsbF identified as a 3-DHS dehydratase, we next sought to determine the efficiency of the AsbF-catalyzed 3-DHS dehydration (3,4-DHBA production) reaction. The reaction rate at room tem-
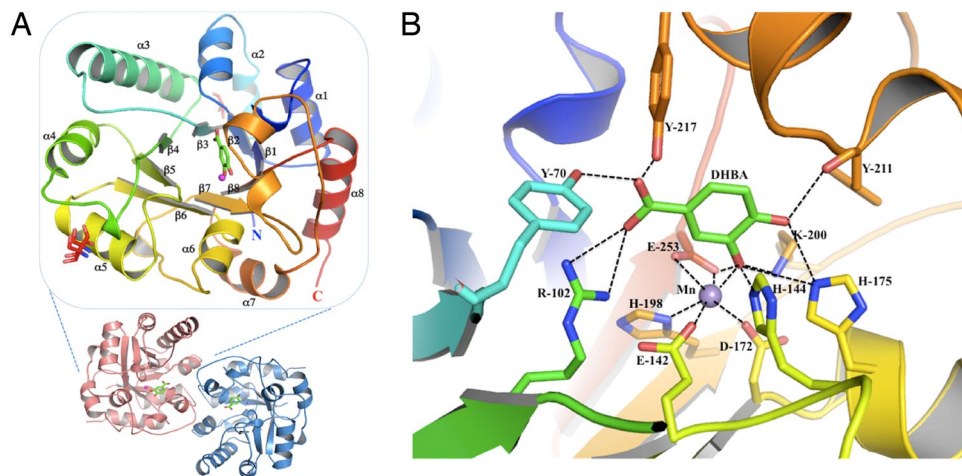
Fig. 2. Structural analysis of AsbF. (*A*) Crystal structure form of AsbF. An overall view of the AsbF monomer is enlarged and rotated 90° relative to the dimeric structure below. Monomer is depicted with a color ramp of blue to red (N to C terminus). The manganese atom is shown as a purple sphere in the middle of the TIM barrel adjacent to the ligand molecule 3,4-DHBA (green). Numbering of main TIM barrel secondary structures is shown as α1–8 and β1–8. (*B*) Active site of liganded AsbF showing 3,4-DHBA coordinated to manganese interacting with side chains. Manganese is coordinated with 4 carboxyl group oxygen atoms from 2 glutamate residues and an aspartate as well as an amine of His ranging in distance between 2.08 and 2.38 Å. All hydrogen bonds are indicated by dashed lines.

perature increased monotonically with increasing pH (from 6.0 to 9.2) with a plateau between 7.2 and 8.0 (Fig. S3*B*). Earlier studies of a fungal 3-DHS dehydratase suggested a requirement for divalent cations (15, 16). Significantly, the AsbF-catalyzed dehydration reaction was inhibited at EDTA concentrations >0.1 mM. Supplementation of this experimental reaction mixture with 5 mM MgCl$_2$ restored activity. After this observation, a suite of metals was titrated into reactions containing AsbF inactivated by EDTA. While a series of divalent cations including cobalt, calcium, and magnesium reactivated the enzyme, manganese was found to maximize catalytic efficiency whereas equal concentrations of zinc completely abrogated it. In conjunction with these biochemical findings, a fluorescent scan of crystallized recombinant AsbF showed manganese to be the predominant enzyme-bound metal (data not shown, see below). Similar dependencies, in which manganese is the preferred metal and zinc is inhibitory, are found among a structural class of sugar isomerases (18).

Kinetic parameters for AsbF at pH 7.5 were determined spectrophotometrically. Recorded initial velocities were fit to a Michaelis–Menten curve demonstrating the enzyme to have a K_m of ≈290 μM and a k_{cat} of ≈80 min^{-1}. The K_m value is on an order of magnitude similar to those reported by groups describing fungal dehydroshikimate dehydratases from *N. crassa* (590 μM) (15) and *A. nidulans* (530 μM) (16).

Structural Characterization of AsbF Bound to Its Product, 3,4-DHBA. Because of the lack of sequence similarity to known 3-DHS dehydratases, we sought the crystal structure of AsbF and to explore a potential reaction mechanism based on these insights. The structure of AsbF adopts a $(\beta/\alpha)_8$-barrel (TIM barrel) configuration (Fig. 2*A*). As expected from a prior TEV protease cleavage experiment (*Materials and Methods*), the N terminus of the structure is partially buried at the bottom part of the barrel whereas the C terminus is completely exposed to the solvent channel. With the His$_6$ tag in place, the C termini could be involved in lattice interactions with neighboring protein molecules, which might have led to twinning.

AsbF belongs to AP endonuclease 2 TIM barrel proteins (19), with the closest homologues including xylose isomerase and the myoinositol catabolism protein IolI (20). The internal section of AsbF is well packed by relatively large side chains with a narrow bottom part of the barrel relative to the top. The barrel opens up

at the top to form a pocket with a number of hydrophilic residues including His, Glu, Thr, Lys, Tyr, and Gln to contain a specific ligand. Unexpectedly, the 3,4-DHBA reaction product was found in the active/binding site of AsbF, surrounded by several aromatic amino acid residues including F255, F211, F104, H144, and Y217. The 3,4-DHBA molecule makes direct contacts with hydroxyl groups of Y70 and Y217, a guanidinium of R102, an amine of K200, an imine of H175, a carboxyl of E253, and the main-chain carbonyl of F211 using mainly hydrogen bonding interactions. Moreover, 3,4-DHBA is capped tightly under the helical loop (residues 206–224) located between the seventh β-strand (β7) and the seventh α-helix (α7) and is directly coordinated with a Mn^{2+} ion that is also found in the structure (Fig. 2*A*). Both 3,4-DHBA and a metal ion were evident from the electron density map calculation using experimental phases with the weighted coefficient (Fw). Metal identity was determined from the specific emission peak during the fluorescence spectrum scan. Inspection of the AsbF structure reveals that Mn^{2+} is coordinated with the carboxylic acid side chains of E142, D172, E253 (both oxygen atoms), the deprotonated imine of H198, and the 3-hydroxy group of 3,4-DHBA, with the distance range of 2.08–2.38 Å that is typical of Mn^{2+} ions (Fig. 2*B*) (21). Although there is only 1 AsbF protein molecule in the asymmetric unit, they apparently form a dimer (Fig. 2*A*) that excludes 2,460 Å of surface area according to PISA (22). Analysis by static light scattering and size-exclusion chromatography also supports a dimeric state of the enzyme in solution (data not shown).

Structural comparisons revealed that AsbF can be reasonably well superimposed with the 3-dehydroquinate dehydratase (DHQ) from *Salmonella typhimurium* (1qfe) (Fig. S4*A*), an enzyme that functions as part of the shikimate pathway for biosynthesis of aromatic compounds (19). Indeed the AsbF structure is generally homologous to this type of dehydratase enzyme comprised of a TIM barrel fold with a few variations, including the lid loop located at the top of the pocket. For AsbF, this lid loop extends from residue 202 to residue 227 as the partly α-helical loop between strands β7 and α7. In contrast, for the enzyme DHQ it comes from the loop between β3 and α3 spanning residues 82–93 covering approximately the opposite side of the pocket mouth. Another important difference in DHQ is an additional small β-ribbon at the C terminus that closes the bottom of the β-barrel. Each ligand in its corresponding binding pocket occupies a different location and orientation (Fig. S4*A*).

Table 1. Kinetic parameters for AsbF mutants

Mutant	K_m, μM	k_{cat}, min^{-1}	% activity
WT	288.72 ± 38.93	79.84 ± 0.96	100
K200E	—	—	Inactive
K200A	—	—	Inactive
K200R	30.25 ± 8.48	2.56 ± 0.05	3.2
H144A	—	—	Inactive
H175A	—	<1	Trace
R102A	—	—	Inactive
Y70A,Y217A	≈2,511	48.35 ± 3.82	60.6

Site-directed mutagenesis was performed on BA 1986 (*asbF*) to probe for residues involved in catalysis. The K_m of WT AsbF is comparable to 2 eukaryotic 3-DHS dehydratases. Inactive mutants are presumably disrupted in coordination of the metal or substrate. Replacement of Y70 and Y217 is likely to expose the active site to solvent and reduce substrate specificity while loss of the proposed catalytic H144 renders the enzyme inactive.

One of the key distinctions between TIM barrel enzymes is the location of metal binding sites and the type of metal involved. The AsbF manganese ion is bound to 6 atoms, including 1 from 3,4-DHBA and 5 amino acid residues that may also contribute to catalysis by stabilizing an intermediate ligand and/or a product ligand differing from other dehydratases, particularly DHQ (such as 1qfe) that does not contain a metal cofactor (19).

Proposed Mechanism for AsbF Dehydratase. With the crystal structure as a guide, we used site-directed mutagenesis to probe further the key amino acid residues involved in catalysis of AsbF. This analysis revealed that a K200R mutant form of the protein was partially active, confirming the lack of a covalent imine intermediate shown to occur in structurally similar DHQs (19). Characterization of additional AsbF site-directed mutants demonstrated (Table 1) that most inactive forms of the enzyme lacked residues believed to be crucial for metal or substrate coordination ascertained through inspection of the 3,4-DHBA orientation within the AsbF crystal structure (Fig. 2*B*).

Based on the crystal structure and mutant analysis, the surrounding amino acid residues comprising the putative AsbF active site suggest an E_1CB (elimination unimolecular via conjugate base) mechanism that requires a base to abstract the axial proton from the adjacent aliphatic carbon atom (C4) of 3-DHS (Fig. 3). In the AsbF structure, H144 is orthogonal to the catechol ring of the 3,4-DHBA product, an ideal position for removal of the C4 axial proton (the hydroxyl is equatorial) of the substrate. H144 and E142 are both well conserved among members of the xylose isomerase family (Fig. S5). The nearby E142 could elevate basicity of H144 by forming a hydrogen bond to NE2 of H144, improving its proton abstraction ability. Histidine functions as a base for initial proton removal during many enzymatic reactions, including some type I 3-dehydroquinate dehydratases (23, 24). Furthermore, although the activity of a H175A mutant is attenuated, the adjacent AsbF H144A mutant

is completely inactive. Proton removal from the C4 position of 3-DHS leads to formation of a noncovalently bound enolate intermediate with the resulting negative charge stabilized by the divalent Mn^{2+} cation.

To assess enolate formation as a first step in conversion of 3-DHS to 3,4-DHBA, we conducted a deuterium labeling experiment using the AsbF reaction in D_2O buffer. Rapid and reversible exchange of deuterium from the conversion of C3 keto to enol (Fig. 3) was expected to result in accumulation of the substrate bearing a 1 mass unit increase detectable by Fourier-transform ion cyclotron resonance MS. This rapid exchange was readily detectable (Fig. S6), supporting the proposed mechanistic hypothesis regarding initial formation of the 3-DHS enolate upon substrate binding to AsbF.

In a second, more rapid step of the reaction, dehydration presumably occurs through a general acid-catalyzed elimination of the C5 hydroxyl and product formation after aromatization (Fig. 3). The most likely candidate for the acid-catalyzed removal of the C5 hydroxyl is the main-chain carbonyl of Y211 located at the C terminus of the short α-helix as a part of the helical loop between $\beta7$ and $\alpha7$ capping the binding pocket. A main-chain carbonyl is generally not a good acid, but the main-chain carbonyl of Y211 is the closest to C5, and its acidity is likely to be elevated by positioning at the C terminus of the α-helix (with partial negative charge from the helix dipole) that includes conserved amino acid residues among the family (Fig. 2*B*).

To understand further the role of specific active-site residues in catalysis, we modeled 3-DHS in place of the 3,4-DHBA in AsbF (Fig. S4*B*). This motivated analysis of Y217 and Y70, which were initially believed to be necessary for excluding solvent from the active site. Both were found to be inconsequential for normal enzymatic function when mutated individually and reduced activity by only 40% when the corresponding double Tyr mutation was constructed (Table 1). Unexpectedly, an R102A mutation completely inactivates AsbF indicating its role in maintaining a proper active-site conformation, whereas substitution of K200 for arginine significantly reduces substrate binding and overall catalytic efficiency.

Elucidation of the AsbF Structure and Function Is Important to Understanding Siderophore Biosynthesis of *B. anthracis*. Recently, other pathogenic *Bacillus* sp. were found to produce petrobactin (6), whereas the ability for uptake and utilization of exogenous petrobactin is even more widespread among prokaryotes (25). Moreover, some evidence suggests that the siderophore or its analogs play additional biological roles beyond iron sequestration (26–28). Although we have now characterized the enzymatic activity of AsbF as well as its role in iron acquisition, the complete nature of the enzyme within bacteria has yet to be fully understood. Indeed research on other members of the *asb* gene cluster suggests that a pool of 3,4-DHBA, and thus functioning AsbF, is necessary for the initial steps of petrobactin biosynthesis (3, 9).

The entire *asb* gene cluster exemplifies the coevolution of a pathogen with its host. AsbF itself, with its metal coordination
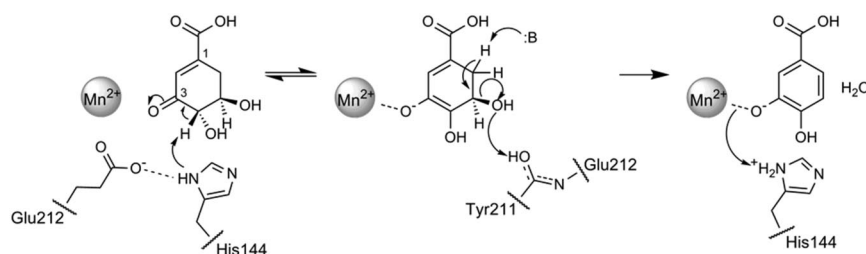

Fig. 3. Proposed mechanism for AsbF-catalyzed conversion of 3-DHS to 3,4-DHBA. Mn^{2+} stabilizes an enolate intermediate after proton removal at C4 by H144. This is followed by dehydration/aromatization of the molecule to generate the key petrobactin subunit 3,4-DHBA.

structure reminiscent of other proteins, most likely evolved from enzymatic precursors with a purpose very different from siderophore biosynthesis. The presence of the unusual 3,4 isomer of DHBA in petrobactin is vital to its ability to acquire iron for the bacterium while avoiding detection by innate host defenses. Without petrobactin, *B. anthracis* would be limited to the ability of bacillibactin to compete for free iron, a process that is highly compromised because of siderocalin sequestration (7). Because the generation of 3,4-DHBA is a key step for petrobactin biosynthesis (9), AsbF represents an attractive target for small-molecule antibiotic therapy. In addition to the prevention of petrobactin assembly, disrupting AsbF function would thwart uptake of any iron bound by 3,4-DHBA subunits that may be exported out of the cell (9). This approach is supported by the fact that *B. anthracis* cells carrying an *asbF* gene deletion grow significantly more poorly in iron-depleted media (3) and display a highly attenuated lethality to mice (Fig. S1). The search for AsbF inhibitors with possible therapeutic application is already underway. Questions regarding how AsbF is regulated and the precise timing and order of 3,4-DHBA incorporation into petrobactin remain to be addressed. This research will serve to further articulate how even insidious microbes are fundamentally reliant on finding a method to surpass innate immune defenses in the acquisition of nutrients and will likely uncover innovative strategies for combating life-threatening infections.

Materials and Methods

Analysis of Sterne Strain Mutants. *B. anthracis asb* mutant strains ΔasbA, ΔasbB, ΔasbC, ΔasbD, ΔasbE, ΔasbF, and ΔasbABCDEF (3) as well as a wild-type Sterne 34F2 were generated as described previously and grown in IDM (3). Filtrates (100 mL) of the growth medium were prepared as described previously (3). Sample preparation for TLC analysis and quantification of 3,4-DHBA were performed by extracting acidified (pH 2.0) IDM culture supernatants (10 mL) with an equal volume of ethyl acetate 3 times. The organic layers were pooled, and the solvents were concentrated to dryness *in vacuo*. The dried pellets were dissolved in 50 μL of methanol and used for analysis. TLC was performed with the extracts on a cellulose plate (Merck). TLC plates were developed with a solvent system of butanol-acetic acid-water (12:3:5, vol/vol/vol), and 3,4-DHBA was detected by spraying with 1% (wt/vol) ferric chloride.

For quantification of 3,4-DHBA (Table S1), samples were analyzed by HPLC. Analytical results and detailed methods are available online in the Table S1 legend.

Intratracheal Inoculation of DBA/2 Mice. Mouse infection was performed as described previously (12). All mouse experiments were performed by using protocols approved by the University of Michigan Committee on the Use and Care of Animals.

Cloning and DNA Manipulation. The *asbF* gene of the *B. anthracis* Sterne strain was cloned into the expression vector pMCSG7 (29) by using ligation-independent cloning (30). Detailed cloning and mutagenesis methods are available in *SI Methods*.

Bioinformatic Analysis. Bioinformatic analyses of the *B. anthracis asb* cluster and homologs were performed with tools implemented within the Integrated Microbial Genomes web site (http://img.jgi.doe.gov) and the EMBL-EBI web site (www.ebi.ac.uk).

Protein Purification for Enzymatic Analysis. All pMCSG7-*asbF* constructs were subsequently used to transform BL21 expression cells (Novagen). The enzyme was purified by using standard His-tag Ni-affinity chromatography. Detailed protein purification methods are available in *SI Methods*.

Enzymatic Assays. Initial substrate determination assays were performed with 75 mM Hepes (pH 7.5), 100 mM substrate (3-DHS), and 1 μM enzyme. Fifty-microliter reactions were tracked spectrophotometrically by observing ΔA_{290} using a SpectraMax M5 plate reader (Molecular Devices). Standard serial dilutions of synthesized 3,4-DHBA (Fluka) in similar reaction conditions were used to quantify product yield. LC-MS analysis of substrate to product conversion was performed by addition of 9 reaction volumes of methanol followed by evaporation of the resulting supernatant and loading onto a 3.5-μm C18 reverse-phase column (Waters) in line with a Shimadzu LCMS-2010A

for detection. Elution was performed with a stepwise 5–70% gradient of MeCN in 20 mM aqueous NH₄HCO₃. Changes to reaction conditions were performed as noted in the text. Characterization of kinetic parameters was performed with 75 mM Hepes (pH 7.5), 250 nM enzyme, and various concentrations (0–2 mM) of 3-DHS in 80-μL reactions. Both substrate and enzyme were equilibrated in reaction buffer at ambient temperature for 15 min before the reaction was initiated by mixing. 3,4-DHBA production was tracked by observing ΔA_{290} using a Flexstation III plate reader (Molecular Devices). Reactions were run in quadruplicate, and nonlinear regression using Kaleidagraph software (Synergy) was performed on a plot of V_0 vs. [3-DHS] for determination of K_m and V_{max}.

Gene Cloning, Expression, and Protein Purification for Structure Determination. After failing to obtain diffraction-quality crystals from the initial pMCSG7-*asbF* construct, *asbF* was cloned in pMCSG26 vectors with 2 variations, including an uncleavable C-terminal His₆ tag and a C-terminal His₆ tag with a TEV protease cleavage site. Recombinant *E. coli* cells for AsbF overexpression were grown by using selenomethionine (Se-Met)-containing enriched M9 medium (pink medium) under conditions known to inhibit methionine biosynthesis (31, 32). Protein was purified by 2-step Ni-affinity chromatography following the standard protocol described previously (33). Detailed cloning, overexpression, and purification methods are available in *SI Methods*.

Protein Crystallization. Crystallization screening was executed for all AsbF protein variants, including the one bearing an N-terminal His₆ tag (expressed from pMCSG7) and the ones from pMCSG26 vectors with and without the C-terminal His₆ tag cleavage. They were screened for crystallization conditions by using a Mosquito robot (TTP Labtech) using sitting drops in 96-well plates (Greiner), with drops of 0.4 μL of protein at 60 mg/mL mixed with 0.4 μL of crystallization screen solutions and equilibrated over 135 μL of crystallization screen solutions in the well at 18 °C. A number of commercially available screens including Index (Hampton Research) and ANL-1 and ANL-2 (Qiagen) were used for crystallization screening. AsbF with N-terminal His₆ tag failed to yield a diffraction-quality crystal. The best crystals of AsbF without the TEV cleavage site appeared after 1–2 days from Index #25 containing 3.5 M sodium formate (pH 7.0). The same condition and a few others including ANL-2 #88 and #89 gave diffraction-quality crystals for the AsbF without the C-terminal His₆ tag. Before data collection crystals were flash-frozen in liquid nitrogen in the presence of a number of different cryoprotectants. The chunky plate shape of a 0.15-mm side crystal of the AsbF with the C-terminal tag diffracted to 2.0 Å. However, the data were twinned, and the phasing stalled. One of the rod-shape crystals of AsbF lacking a His₆ tag from condition ANL-2 #89 (0.1 M Tris, pH 8.5/3.2 M sodium chloride) with the saturated sucrose cryoprotectant diffracted to 2.12 Å and was used for data collection.

Table 2. AsbF data collection, phasing and refinement

Data Collection (anomalous peak)

Wavelength, Å	0.9793
Resolution (last shell), Å	49.4 to 2.11 (2.19 to 2.11)
Reflections measured/unique	22,726/2,210
Multiplicity	13.9 (12.3)
Completeness (last shell), %	99.9 (99.4)
R sym (last shell), %*	14.4 (53.4)
I/σ (last shell)	9.1 (7.1)
Phasing	
Resolution, Å	49.4 to 2.12
Phasing power	1.06
Figure of merit	0.112
After density modification	0.801
Refinement	
Resolution, Å	49.4 to 2.12
R work/R free†	14.8/17.8
rms deviation bond lengths, Å	0.017
rms deviation bond angles, Å	1.47
PDB code	3DX5

*$R_{sym} = \Sigma\Sigma j\ Ij - <I> /\Sigma Ij$, where Ij is the intensity measurement for reflection j, and $<I>$ is the mean intensity for multiply recorded reflections.

†$R_{work}/R_{free} = \Sigma\|F_{obs} - F_{calc}\|/F_{obs}$, where the working and free R factors are calculated by using the working and free reflections sets. The free reflections (5% of the total) were held aside throughout refinement.

Data Collection, Structure Determination, Refinement, and Deposition. The single-wavelength anomalous dispersion (SAD) data near the Se absorption edge (0.9793Å) up to 2.12 Å were collected from a single Se-Met-labeled rod-shape protein (30 × 30 × 300 μm) crystal at 100 K at the 19ID beam line of the Structural Biology Center at the Advanced Photon Source, Argonne National Laboratory. The crystal was exposed for 5 s per 1.0° rotation of ω with the crystal to detector distance of 320 mm. The data were recorded on an ADSC Q315 detector by the scanning of 200°. The space group was $P6_522$ with cell dimension of $a = b = 134.48$ Å and $c = 72.81$ Å. All data were processed and scaled with HKL3000 (34) (Table 2).

The structure was determined by SAD phasing using the anomalous signal from Se atoms with HKL3000 (34), SHELX (35), SOLVE/RESOLVE (36), MLPHARE (37), DM (38), CCP4 (39), and arp/Warp (40) using the peak data to 2.12 Å. The model from HKL3000 after the high-resolution model building routine by arp/Warp contained most of the residues with side chains except 4 N-terminal residues, 7 C-terminal residues, and all artificial residues from cloning. The extra electron density for the 3,4-DHBA was evident from the electron density map calculated from the experimental phases. The subsequent refinement was performed iteratively by REFMAC 5.2 (41) in CCP4 and manual adjustment using Coot (42) until it converged to the R factor of 0.148 and the free R of 0.178 with the rms bond distances of 0.017 and the rms bond angles of 1.47°. The final model included residues 1–274 of 1 chain of AsbF, 1 molecule of 3,4-DHBA, a Mn ion, a disordered Tris, a glycerol molecule, and 320 ordered water molecules. The C terminus residues including those introduced during cloning could not be resolved. The stereochemistry of the structure was checked with PROCHECK (43) and the Ramachandran plot. Atomic coordinates and experimental structure factors of AsbF have been deposited in the Protein Data Bank under ID code 3DX5.

Supporting Information. For full experimental details, see *SI Methods*, Table S1, and Figs. S4–S6.

1. Andrews SC, Robinson AK, Rodriguez-Quinones F (2003) Bacterial iron homeostasis. *FEMS Microbiol Rev* 27:215–237.
2. Koppisch AT, *et al.* (2005) Petrobactin is the primary siderophore synthesized by *Bacillus anthracis* str. Sterne under conditions of iron starvation. *Biometals* 18:577–585.
3. Lee JY, *et al.* (2007) Biosynthetic analysis of the petrobactin siderophore pathway from *Bacillus anthracis*. *J Bacteriol* 189:1698–1710.
4. Wilson MK, Abergel RJ, Raymond KN, Arceneaux JE, Byers BR (2006) Siderophores of *Bacillus anthracis*, *Bacillus cereus*, and *Bacillus thuringiensis*. *Biochem Biophys Res Commun* 348:320–325.
5. Cendrowski S, MacArthur W, Hanna P (2004) *Bacillus anthracis* requires siderophore biosynthesis for growth in macrophages and mouse virulence. *Mol Microbiol* 51:407–417.
6. Koppisch AT, *et al.* (2008) Petrobactin is produced by both pathogenic and non-pathogenic isolates of the *Bacillus cereus* group of bacteria. *Biometals* 21:581–589.
7. Abergel RJ, *et al.* (2006) Anthrax pathogen evades the mammalian immune system through stealth siderophore production. *Proc Natl Acad Sci USA* 103:18499–18503.
8. Fischbach MA, Lin H, Liu DR, Walsh CT (2006) How pathogenic bacteria evade mammalian sabotage in the battle for iron. *Nat Chem Biol* 2:132–138.
9. Pfleger BF, *et al.* (2007) Characterization and analysis of early enzymes for petrobactin biosynthesis in *Bacillus anthracis*. *Biochemistry* 46:4147–4157.
10. Garner BL, Arceneaux JE, Byers BR (2004) Temperature control of a 3,4-dihydroxyben-zoate (protocatechuate)-based siderophore in *Bacillus anthracis*. *Curr Microbiol* 49:89–94.
11. Koppisch AT, *et al.* (2008) Biosynthesis of the 3,4-dihydroxybenzoate moieties of petrobactin by *Bacillus anthracis*. *J Org Chem* 73:5759–5765.
12. Fisher N, *et al.* (2006) The *dltABCD* operon of *Bacillus anthracis* Sterne is required for virulence and resistance to peptide, enzymatic, and cellular mediators of innate immunity. *J Bacteriol* 188:1301–1309.
13. Hosokawa K, Stanier RY (1966) Crystallization and properties of p-hydroxybenzoate hydroxylase from *Pseudomonas putida*. *J Biol Chem* 241:2453–2460.
14. Frost JW, Draths KM (1995) Biocatalytic syntheses of aromatics from D-glucose: Renewable microbial sources of aromatic compounds. *Annu Rev Microbiol* 49:557–579.
15. Stroman P, Reinert WR, Giles NH (1978) Purification and characterization of 3-dehydroshikimate dehydratase, an enzyme in the inducible quinic acid catabolic pathway of *Neurospora crassa*. *J Biol Chem* 253:4593–4598.
16. Wheeler KA, Lamb HK, Hawkins AR (1996) Control of metabolic flux through the quinate pathway in *Aspergillus nidulans*. *Biochem J* 315:195–205.
17. Yi J, Li K, Draths KM, Frost JW (2002) Modulation of phosphoenolpyruvate synthase expression increases shikimate pathway product yields in *E. coli*. *Biotechnol Prog* 18:1141–1148.
18. Fuxreiter M, Farkas O, Naray-Szabo G (1995) Molecular modelling of xylose isomerase catalysis: The role of electrostatics and charge transfer to metals. *Protein Eng* 8:925–933.
19. Gourley DG, *et al.* (1999) The two types of 3-dehydroquinase have distinct structures but catalyze the same overall reaction. *Nat Struct Biol* 6:521–525.
20. Zhang RG, *et al.* (2002) Crystal structure of *Bacillus subtilis* IolI shows endonuclease IV fold with altered Zn binding. *Proteins* 48:423–426.
21. Zheng H, Chruszcz M, Lasota P, Lebioda L, Minor W (2008) Data mining of metal ion environments present in protein structures. *J Inorg Biochem* 102:1765–1776.
22. Krissinel E, Henrick K (2007) Inference of macromolecular assemblies from crystalline state. *J Mol Biol* 372:774–797.
23. Deka RK, Kleanthous C, Coggins JR (1992) Identification of the essential histidine residue at the active site of *Escherichia coli* dehydroquinase. *J Biol Chem* 267:22237–22242.
24. Leech AP, *et al.* (1998) Re-evaluating the role of His-143 in the mechanism of type I dehydroquinase from *Escherichia coli* using two-dimensional ^{1}H,^{13}C NMR. *J Biol Chem* 273:9602–9607.
25. Abergel RJ, Zawadzka AM, Raymond KN (2008) Petrobactin-mediated iron transport in pathogenic bacteria: Coordination chemistry of an unusual 3,4-catecholate/citrate siderophore. *J Am Chem Soc* 130:2124–2125.
26. Gardner RA, Kinkade R, Wang C, Phanstiel O (2004) Total synthesis of petrobactin and its homologues as potential growth stimuli for *Marinobacter hydrocarbonoclasticus*, an oil-degrading bacteria. *J Org Chem* 69:3530–3537.
27. Harris WR, Amin SA, Kupper FC, Green DH, Carrano CJ (2007) Borate binding to siderophores: Structure and stability. *J Am Chem Soc* 129:12263–12271.
28. Hickford SJ, *et al.* (2004) Petrobactin sulfonate, a new siderophore produced by the marine bacterium *Marinobacter hydrocarbonoclasticus*. *J Nat Prod* 67:1897–1899.
29. Stols L, *et al.* (2002) A new vector for high-throughput, ligation-independent cloning encoding a tobacco etch virus protease cleavage site. *Protein Expression Purif* 25:8–15.
30. Aslanidis C, de Jong PJ (1990) Ligation-independent cloning of PCR products (LIC-PCR). *Nucleic Acids Res* 18:6069–6074.
31. Van Duyne GD, Standaert RF, Karplus PA, Schreiber SL, Clardy J (1993) Atomic structures of the human immunophilin FKBP-12 complexes with FK506 and rapamycin. *J Mol Biol* 229:105–124.
32. Walsh MA, Dementieva I, Evans G, Sanishvili R, Joachimiak A (1999) Taking MAD to the extreme: Ultrafast protein structure determination. *Acta Crystallogr D* 55:1168–1173.
33. Kim Y, *et al.* (2004) Automation of protein purification for structural genomics. *J Struct Funct Genomics* 5:111–118.
34. Minor W, Cymborowski M, Otwinowski Z, Chruszcz M (2006) HKL-3000: The integration of data reduction and structure solution—From diffraction images to an initial model in minutes. *Acta Crystallogr D* 62:859–866.
35. Sheldrick GM (2008) A short history of SHELX. *Acta Crystallogr A* 64:112–122.
36. Terwilliger TC (2003) Automated main-chain model building by template matching and iterative fragment extension. *Acta Crystallogr D* 59:38–44.
37. Otwinowski Z (1991) *Daresbury Study Weekend Proceedings*, eds Wolf W, Evans PR, Leshe AGW (SERC Daresbury Laboratory, Warrington, UK), pp 80–85.
38. Cowtan KKC (1994) An automated procedure for phase improvement by density modification. *Joint CCP4 ESF-EACBM Newslett Protein Crystallogr* 31:34–38.
39. Collaborative Computational Project, Number 4 (1994) The CCP4 suite: Programs for protein crystallography. *Acta Crystallogr D* 50:760–763.
40. Morris RJ, Perrakis A, Lamzin VS (2003) ARP/wARP and automatic interpretation of protein electron density maps. *Methods Enzymol* 374:229–244.
41. Murshudov GN, Vagin AA, Dodson EJ (1997) Refinement of macromolecular structures by the maximum-likelihood method. *Acta Crystallogr D* 53:240–255.
42. Emsley P, Cowtan K (2004) Coot: Model-building tools for molecular graphics. *Acta Crystallogr D* 60:2126–2132.
43. Laskowski RA, MacArthur MW, Moss DS, Thornton JM (1993) PROCHECK: A program to check the stereochemical quality of protein structures. *J Appl Crystallogr* 26:283–291.